Cell shape regulates subcellular organelle location to control short-term Ca^{2+} signal dynamics in VSMC

Authors: Rhodora C. Calizo[1], Amit Ron[2], Mufeng Hu[2], Smiti Bhattacharya[2], William G.M. Janssen[1], James Hone[2], Suzanne Scarlata[3], Padmini Rangamani[4]*, and Ravi Iyengar[1]*

One Sentence Summary: The physical interplay of the curvature of the plasma membrane and global cell shape alters the distances between subcellular organelles, which in turn modulates the strength of Ca^{2+} signaling in vascular smooth muscle cells.

Affiliations:

[1]Department of Pharmacological Sciences and Systems Biology Center New York, Icahn School of Medicine at Mount Sinai, New York, NY 10029

[2]Department of Mechanical Engineering, Columbia University, New York, NY 10027

[3]Department of Chemistry and Biochemistry, Worcester Polytechnic Institute, Worcester, MA 01609

[4]Department of Mechanical and Aerospace Engineering, University of California San Diego, La Jolla, CA 92093

Address correspondence to:

Ravi Iyengar, Ph.D.
Department of Pharmacological Sciences
Icahn School of Medicine at Mount Sinai
One Gustave L. Levy Place, Box 1215
New York NY 10029
Phone: 212-659-1707
Fax: 212-831-0114
e-mail: ravi.iyengar@mssm.edu

or

Padmini Rangamani, Ph.D.
Department of Mechanical and Aerospace Engineering
University of California San Diego
La Jolla, CA 92093
Phone: 858-534-4734
e-mail: prangamani@ucsd.edu

ABSTRACT

The shape of the cell is intimately connected to its function; however, we do not fully understand the underlying mechanism by which global shape regulates cell function. Here, using a combination of theory, experiments and simulation, we investigated how global cell shape can affect subcellular organization, and consequently intracellular signaling, to control information flow needed for phenotypic function. We find that global cell curvature regulates the location of the sarcoplasmic reticulum, inter-organelle distances and differential distribution of receptors in the plasma membrane. A combination of these factors leads to the modulation of signals transduced by the M_3 muscarinic receptor/G_q/PLCβ pathway at the plasma membrane, amplifying Ca^{2+} dynamics in the cytoplasm and the nucleus resulting in phenotypic changes, as determined by increased activity of myosin light chain kinase in the cytoplasm and enhanced nuclear localization of the transcription factor NFAT. Taken together, our observations show a systems level phenomenon whereby global cell shape affects subcellular organization and signaling to enable phenotypic changes.

INTRODUCTION

Cells utilize receptors on the plasma membrane to transduce a range of extracellular signals to regulate function in the cytoplasm and the nucleus[1]. Reaction kinetics of the biochemical interactions that comprise the signaling networks regulate the temporal dynamics of activation and inactivation of signaling components and effectors[2]. However, information flow within cells is not just temporally regulated, it is also spatially regulated by the shape of the cell[3-5] and surface-to-volume ratio at the plasma membrane[6]. An additional layer of complexity is conferred by the spatial transfer of information by signaling reactions that occur within or at intracellular organelles. Recently, studies have shown that signaling at the endosomes plays an important role in prolonging cAMP dynamics through GPCRs[7] and in EGFR dynamics[8]. An important compartmental regulation of organelle-based signaling is Ca^{2+} dynamics, since endoplasmic/sarcoplasmic reticulum is a regulatable Ca^{2+} store in cells. Ca^{2+} is a ubiquitous signaling molecule that controls many cellular functions including fertilization, proliferation, migration and cell death[9-12]. Ca^{2+} is able to participate in controlling this diverse array of functions due to the precise control of Ca^{2+} concentration within the cell. In vascular smooth muscle cells (VSMC), Ca^{2+} regulates both contractility and gene expression through IP_3-mediated Ca^{2+} release by IP_3R receptors located on the membrane of the sarcoplasmic reticulum (SR) and through Ca^{2+} influx at the plasma membrane[13-15]. Ca^{2+}-calmodulin activates myosin light chain kinase (MLCK), which phosphorylates the light chain of myosin, initiating contraction[16]. Ca^{2+} also activates protein kinases and phosphatases that regulate transcription regulators that define the phenotypic status of VSMC[17]. Ca^{2+} activates calcineurin, which dephosphorylates the transcription factor nuclear factor of activated T-cells (NFAT) in the cytoplasm, resulting in its nuclear accumulation and expression of NFAT-regulated genes[18]. Ca^{2+} also activates calmodulin kinase II (CaMKII), that phosphorylates the transcription factor serum response factor (SRF)[19] which, as a complex with myocardin, controls the expression of proteins necessary for the contractile function of VSMC[20].

VSMC in the medial layer of blood vessels are not terminally differentiated and can undergo phenotypic transitions during injury and disease states[21-23]. VSMC shape and function are closely related; increasing elongation or aspect ratio (AR, defined as the ratio of the short axis to long axis) is correlated with differentiation and contractility[24, 25]. Previous studies have shown that changes in cell shape mediate major changes in subcellular organization, which may have major consequences in cell physiology and phenotype including contractility, proliferation and differentiation states[26-29]. However, the mechanistic link between cell elongation and changes in phenotype, such as contractility, remains poorly understood. Based on the observations that cell shape and Ca^{2+} signaling closely regulate the contractile phenotype of differentiated VSMCs, we hypothesized that cell shape regulates organelle location, including the relative distances between plasma membrane, endoplasmic/sarcoplasmic reticulum (ER/SR) and the nucleus, to modulate cellular functions. We sought to answer the question -- how does cell shape dependent organelle localization drive spatial control of information flow? The answer to this question is critical for understanding how mechano-chemical relationships control cell shape, signaling, and phenotype. We used 3D biochips to culture VSMCs in different shapes and developed theoretical and computational models to represent the spatio-temporal dynamics of Ca^{2+} transients mediated by Muscarinic Receptor 3 (M_3R)/Phospholipase Cβ (PLCβ) pathway. Activation of M_3R

mediates contractility in VSMC by activating PLCβ resulting in phosphoinositide hydrolysis and IP_3 mediated Ca^{2+} release from the SR[30, 31]. Our studies show an unexpected modulation of organelle location as a function of membrane curvature and that this change in organelle location results in signal amplification in the cytoplasm and nucleus.

RESULTS

Reaction-Diffusion model predicts that the distance between PM and SR membrane affects signaling dynamics in the cytoplasmic volume.

We tested the hypothesis that a change in membrane curvature and distance between two membranes affects signaling dynamics using a phenomenological reaction-diffusion model (Fig. 1a). A signaling molecule of interest, A, is produced at the PM with an on-rate k_{on} (1/s) and binds to a receptor located at the SR membrane, with a rate k_{off} (1/s) and is free to diffuse in the sandwiched cytoplasmic space and is degraded by a degrading enzyme with a rate k_{deg} (1/s). This model essentially captures the lifecycle of a second messenger such as IP_3 that is produced at the PM through PIP_2 hydrolysis by phospholipases, binds to inositol 3 phosphate receptor (IP_3R) channel at the SR membrane and is degraded in the cytoplasm by 1,4,5-trisphosphate-5-phosphatase[32]. These events can be mathematically represented by the following system of reaction-diffusion equations. The dynamics of A in the cytoplasm are governed by diffusion and degradation and is given by,

$$\frac{\partial C_A}{\partial t} = D\nabla^2 C_A - k_{deg} C_A \quad \text{Eq. (1)}$$

Here, D is the diffusion coefficient of A ($\mu m^2/s$), and C_A is the concentration of A (μM). The boundary condition at the PM is a balance between the rate of production of A at the membrane and the diffusive flux from the membrane to the cellular interior and is given by,

$$D(\mathbf{n} \cdot \nabla C_A)|_{PM} = k_{on} C_A|_{PM} \quad \text{Eq. (2)}$$

Here, n is the normal vector to the surface and ∇ represents the gradient operator. At the SR membrane, similarly, we can write the boundary condition for the consumption of A as the balance of diffusive flux to the SR and consumption rate at the SR.

$$-D(\mathbf{n} \cdot \nabla C_A)|_{SR} = k_{off} C_A|_{SR} \quad \text{Eq. (3)}$$

For illustrative purposes, we solved these equations using finite element methods on three geometries (1) a rectangle (constant distance, zero curvature) (2) a circle, (constant distance, constant curvature) and (3) an elliptical sector, (varying distance, varying curvature) (Fig. 1b). In cases (1-2), the gradient of A is only along the radial direction (Fig. 1c). In triangular and trapezoidal geometries, varying PM-SR gradients result in two-dimensional gradients (Supplementary Fig. 1). However in case (3), the curvature of the membrane and the PM-SR distance will affect both the production and consumption of A at the PM and SR respectively. Hence, A varies both in the radial and angular directions, indicating that curvature and varying distances between the two membranes amplifies signaling gradients. Even though the observations here are in 2D, the effect of curvature and distance holds true in 3D as well as has been demonstrated by us and others[3, 33, 34].

We next conducted dimensional analysis to identify when the dynamics of A would be diffusion-dominated or reaction-dominated. Non-dimensionalization of Eq. 1 results in a dimensionless group $D/(k_{deg}L^2)$, the Damkohler number[35]. This dimensionless number is the ratio of diffusion time scale to reaction time scale. We found that the dynamics of A are diffusion dominated for physiological values of k_{deg} (Fig. 1d). Increasing k_{deg} many-fold or reducing the diffusion constant of A can result in the dynamics of A being reaction dominated for different PM-SR distances (Fig. 1d, shaded blue region). Both the increase in k_{deg} and the decrease in D, to obtain reaction-dominated regimes, are out of the range of physiological values, suggesting that the dynamics of A in the sandwiched space between the PM and SR are primarily diffusion dominated. From this simple phenomenological model, we predict that second messenger signaling networks such as IP_3, where signaling occurs between PM and SR, will be impacted by global curvature and distance between the PM and the SR. This prediction raises the following questions: (1) does cell shape affect PM-SR distance? (2) Does changing PM-SR distance affect intracellular signaling dynamics? And (3) what is the impact of changing the distances between organelles on IP_3/Ca^{2+} signaling dynamics?

We asked the question how changing the PM-SR distances can impact the dynamics of IP3 signaling. Since it is currently not possible to experimentally manipulate PM-SR distances with precise control in cells, we used numerical models of IP_3 and Ca^{2+} in the context of VSMC to study the relationship between PM-SR distances and IP3 dynamics. This model is composed of a system of multi-compartmental partial differential equations, representing the reaction-diffusion of cytoplasmic species in the volume, coupled with boundary fluxes at the membrane. The reactions capture the biochemical interactions from the ligand binding and activation of M_3R to IP_3 production by PLC-mediated hydrolysis of PIP_2 release from the SR (Fig. 2a, Supplementary Table 1-2).

In order to investigate how PM-SR distances affect IP_3 dynamics, we constructed a cylindrical geometry to represent a portion of the cell and the ER as discs (Fig. 2b). This idealized geometry enables us to study reaction-diffusion in 3D. We varied the following parameters (a) PM-SR distance, (b) diffusion constant of IP_3, and (c) IP_3 degradation rate. These three parameters govern the production, diffusion, and consumption of IP_3. Our results can be summarized as follows –across all parameter variations, shorter distances between PM-SR gave rise to high IP_3 gradients (Fig 2c i, iv, and vii). Increasing the diffusion coefficient resulted in rapid dissipation of the gradient and increasing IP_3 degradation rate resulting in a lower concentration of IP_3, as expected. We found that the shortest distance between the PM-SR (50 nm), with the smallest diffusion coefficient (10 $\mu m^2/s$), and largest IP_3 degradation rate (0.0625 s^{-1}) (Fig. 2c vii, top row) had the strongest IP_3 gradient at 5s. Increasing the PM-SR distance to 100 nm altered the extent of the observed IP_3 gradient at 5s (Fig. 2c i, bottom row) but did not alter this gradient very much at later times. From these simulations, we predict that changing the distances between organelles alters IP_3 and Ca^{2+} signaling dynamics. We used VSMCs grown on 3D biochips to validate these predictions.

Cell shape affects cytoskeleton organization and organelle location

We determined if changing the cell shape affects organelle distribution. In order to control the large scale cell shape, we used 3D biochips with the same surface area but increasing aspect ratio (AR, circles 1:1 to ellipses 1:8) (Fig. 3a). We investigated how cell shape affects cytoskeletal organization since the two are tightly interwoven[36-38]. Actin stress fibers increasingly oriented

themselves along the long axis of the cell as the aspect ratio increased (Fig. 3b), indicating that the cells were responding to the mechanical forces and tension exerted by the substrate[39]. It has been shown in several cell types that nuclear shape is tightly coupled to cell shape[40]. Nuclear aspect ratio increased with cellular aspect ratio (Fig. 3c-d) while nuclear size (area, in μm^2) decreased with increasing cell aspect ratio (Fig. 3e). The nuclei became increasingly oriented along the major axis of the cell as the whole-cell aspect ratio increased, evidenced by polar graphs showing the orientation histograms of nuclei of cells in increasing cell AR (Fig. 3f). Circular shaped cells showed a random nuclear orientation whereas increasing the cellular aspect ratio progressively oriented the nucleus in the geometric center of the cell. PM-nuclear distance in the major axis of the cell increased with cell aspect ratio (Fig. 3h) while the PM-nuclear distance in the minor axis decreased with cell aspect ratio (Fig. 3i). These results indicate that in VSMC, cell elongation resulted in nuclear elongation, reduced nuclear size, and a decrease in the PM-nuclear distance in the minor axis of the cell (*i.e.* near the center of the cell). In addition to the nucleus, spatial arrangement of the microtubules also changed with aspect ratio. Microtubules became highly aligned and increasingly sparser in the cell tips compared to the cell body as the cell aspect ratio increased (Supplementary Fig. 2). Because cytoskeletal organization plays an important role in the distribution of many organelles[41, 42], we visualized the effect of cell shape on the bulk distribution and location of the mitochondria (Supplementary Fig. 3), endosomes (Supplementary Fig. 4) and Golgi membrane (Supplementary Fig. 5). These organelles increasingly localized to the cell center (perinuclear region) with increasing aspect ratio, similar to the characteristic central distribution of the endomembrane system in well-differentiated VSMC[24]. Because SR stores Ca^{2+}, which controls both excitation-transcription coupling and contractility in VSMC[43], we focused on SR distribution as a function of cell shape, using calnexin (Fig. 3j), protein disulfide isomerase (Fig. 3k), reticulon-4 (Fig. 3l) and bodipy glibenclamide (Supplementary Fig. 6) as SR markers. All four markers show that in circular cells, the SR was spread uniformly throughout the cell; increased aspect ratio induced the SR to localize in the perinuclear region and become significantly sparser, and mainly tubular, in the cell tips (Fig. 3j-l, Supplementary Fig. 6). Upon close inspection of Airy scan images of these SR markers, we qualitatively observe that in circular cells, the SR appeared to be equidistant from the plasma membrane along the periphery, i.e. there were no angular variations of PM-SR distance, while elliptical cells show a large angular variation in the PM-SR distance (Fig. 3d-e bottom panels and Supplementary Fig. 6, inset). Thus, we show that cell shape affects not only cytoskeletal organization, but also affects nuclear shape and PM-nuclear distances, and organelle distribution.

Cell shape changes PM-SR distances in 3D.

Two-dimensional images of peripheral SR membrane and plasma membrane indicate that cell shape alters SR abundance and PM-SR distance on the equatorial region (Fig. 3j-l). We investigated more closely whether PM-SR distances are altered by the global shape of cells in 3D. Confocal volume scans of VSMC cultured in circular and ellipse patterns show increased co-localization between calnexin and plasma membrane stains in the equatorial region of elongated cells, as opposed to the cell tips of elongated cells and circular cells, suggesting increased proximity of the two membranes at the equatorial region of elongated cells (Fig. 4a). Super – resolution STED measurements reveal that SR puncta are closer to the cell cortex in the equatorial region of elongated cells (upper right panel, Fig. 4b), compared to both cell tips of elongated and circular cells (upper left and lower right panels, Fig. 4b). To quantitatively

confirm that the PM-SR distance is shape dependent, we used transmission electron microscopy to visualize peripheral SR to PM distance. TEM showed that the cell periphery of circular cells and the cell body of elliptical cells showed long patches of smooth SR that were positioned close to the plasma membrane. PM-SR distance was indeed dependent on the shape of the cell: PM-SR distance in cell body of elliptical cells was significantly smaller compared to circular cells (Fig. 4c). In the tips of elliptical cells, the SR membrane formed fewer contacts with the plasma membrane, and showed significantly higher PM-SR distance (Fig. 4d). These results are consistent with the recent observation in neurons that PM-ER contacts are more extensive in the cell body compared to elongated projections such as dendrites and axons[44]. While other groups have reported that cell shape can affect organelle location[40, 45], here, we quantitatively determine PM-SR distances and the SR abundance along the juxtamembrane region with controlled cell shape variation.

Cell shape affects receptor activation on the membrane and intracellular calcium dynamics

We tested the model predictions that distance between PM and SR can affect the dynamics of Ca^{2+} mediated by the $M_3R/IP_3/Ca^{2+}$ pathway[13, 46]. We stained for M_3R in circular and elliptical cells under three different conditions - unstimulated, stimulated with carbachol, and stimulated with carbachol in the presence of hypertonic sucrose, which inhibits receptor endocytosis[47-49]. In both the basal state and stimulated states, M_3R was uniformly distributed on the plasma membrane of both circular and elliptical cells (Supplementary Fig. 9). Interestingly, in elliptical cells, when M_3R was stimulated and endocytosis was inhibited, M_3R accumulated in the cell body compared to the cell tips while there was no observable spatial asymmetry in the distribution of M_3R in circular cells (Fig. 5a and Supplementary Fig. 9). We then investigated the effect of shape on cytoplasmic and nuclear Ca^{2+} dynamics upon stimulation of M_3R in patterned VSMC (Fig. 5b-c). In the cytoplasmic region, circular and elliptical showed similar peak Ca^{2+} amplitudes. However, elliptical cells showed a slower rate of decrease in Ca^{2+} compared to circular cells, resulting in a reproducibly observable higher temporally integrated Ca^{2+} compared to circular cells, although the differences were not statistically significant ($p=0.057$, two-tailed t-test). Since small changes in second messenger signals can have large functional effects by being amplified by signaling networks[50], we measured downstream effector activities in the cytoplasm and in the nucleus. We measured myosin light chain kinase (MLCK) activity using a CaM-sensor FRET probe[51, 52] (Fig. 5e-g) to obtain estimates of actin cytoskeletal dynamics associated with contractility. Elliptical cells showed a higher degree of MLCK FRET probe localization on actin filaments (Fig. 5e) and higher maximal activation compared to circular cells (Fig. 5f-g), indicating that the shape-induced increase in cytoplasmic Ca^{2+} signal propagates and is amplified downstream through MLCK activation to control contractility. This is consistent with the previous finding that higher aspect ratio VSMC are more contractile[27, 53]. This observation supports the relationship between cell shape, Ca^{2+} signaling and contractility which has been demonstrated by previous studies [27, 28]. The novelty of our observations is that this effect is correlated with the differences in the distance of the organelles.

The differences in nuclear Ca^{2+} between circular and elliptical cells were distinct from cytoplasmic Ca^{2+} (Fig. 5h). In the nuclear region, the peak Ca^{2+} amplitudes of circular and elliptical cells were similar. However, there is a notable delay in the rate of nuclear Ca^{2+} increase to maximum in elliptical cells compared to circular cells, and the decay times in elliptical cells were slower as well, resulting in a significantly higher concentrations of temporally integrated

Ca^{2+} in elliptical cells compared to circular cells (Fig. 5i). These results indicate that cell shape affects nuclear Ca^{2+} transients triggered by M_3R/PLCβ and that such transients are more prolonged in elliptical cells. Increase in nuclear Ca^{2+} in elliptical cells is likely to impact the nucleo-cytoplasmic transport of NFAT, which exhibits a Ca^{2+}/calcineurin dependent translocation and residence time in the nucleus[18, 54]. We measured NFAT-GFP localization dynamics in live VSMCs in elliptical and circular 3D biochips in response to $G\alpha_q$ activation through M_3R stimulation (Fig. 5j-m). Elliptical cells exhibited greater NFAT-GFP nuclear localization compared to circular cells (Fig. 5k) and on average displayed higher maximal $NFAT_{nuc/cyto}$ (Fig. 5l). We independently validated these differences in NFAT localization by immunofluorescent antibody-based visualization of NFAT1 (Fig. 5m, Supplementary Fig. 10a). At basal levels, $NFAT_{nuc/cyto}$ were similar between circular and elliptical cells. However, elliptical cells displayed higher nuclear NFAT compared to circular cells at 30 minutes and 1 hour after stimulation, consistent with live-cell NFAT-GFP translocation results. To determine whether the effects of Ca^{2+} were general, we studied the localization of SRF in the nucleus. Ca^{2+} also triggers the nuclear localization of SRF through nuclear Ca^{2+}/CaMKIV[19] and actin dynamics[55, 56]. Elliptical VSMC show increased nuclear SRF compared to circular cells at both basal and stimulated levels (Supplementary Fig. 10b). In contrast there was no difference in the localization of myocardin, a transcription factor known to be unaffected by Ca^{2+} dynamics, between circular and elliptical cells (Supplementary Fig. 10c). Myocardin has been shown to be constitutively active[20, 57]. Taken together, these results indicate that shape-induced modulation of Ca^{2+} signaling alters Ca^{2+} dependent physiological activities in both the cytoplasm and the nucleus.

An integrated model of shape and organelle location provides insight into curvature coupling of Ca^{2+} dynamics in VSMCs.

Thus far, we have focused on 3D simulations in small portions of the cell to study the effect of PM-SR distance on IP3 dynamics (Fig. 2). However, recent ultrastructural analyses have shown that the ER is a highly dynamic, tubular network that occupies roughly 10% of the cytosolic volume and extends from the nucleus to the cell periphery[58]. In order to consider both cell shape (Fig. 3) and the extent of the PM-SR distance, we developed a larger length scale, multi-compartmental partial differential equation model in *COMSOL* (Fig. 6a-g) and *Virtual Cell* (Fig. 6h-y) to derive relationships between experimental observations and models at the length scale of the whole cell.

To represent the cell with a circular cross section (Fig. 6a-b), we use an oblate spheroid and the SR were represented as a series of toroids within the spheroid. We represented the cell with an elliptical cross section with an ellipsoid with no axes of symmetry and the SR was modeled as tubes running along the circumference of the cell (Fig. 6c-d). We used these geometries to simulate IP_3 transients and observed that even in these large length scale simulations, the effect of shape was immediately apparent – the oblate spheroid displayed a gradient in the radial direction at any cross section but not in the angular direction. However, the ellipsoid-shaped geometry displayed gradients both in the radial and angular direction, demonstrating that cell shape coupled with PM-SR distance does indeed affect the spatio-temporal dynamics of IP_3. Indeed these effects can be observed even in simplified 2D geometries in both circles and ellipses (Fig. 6f-h). The cell was represented in *Virtual Cell* as nested ellipsoids with varying aspect ratios (Fig. 6i). Upon stimulation of the $M_3R/IP_3/Ca^{2+}$ pathway, the concentration

gradients of IP_3 and cytoplasmic Ca^{2+} were highest in regions where PM-SR distance was lowest (cell body), and lowest in regions where PM-SR were farthest from each other (cell tips) (Fig. 6j and Fig. 6m), establishing an IP_3 and Ca^{2+} gradient from the cell body to the tips which progressively became steeper with aspect ratio. More importantly, increasing the AR increased global IP_3 and Ca^{2+} levels in both cytoplasmic and nuclear compartments (Fig. 6k-l, Fig. 6n-o, Fig. 6q-r). Hence, ellipsoid cells are predicted to exhibit increased global cytoplasmic and nuclear Ca^{2+} compared to circular cells upon stimulation of M_3R due to decreased PM-SR and PM-nuclear distance in the short axis of the cell. Corresponding 2D spatio-temporal models of IP_3, cytoplasmic Ca^{2+} and nuclear Ca^{2+} also captured the shape dependent gradient formation of signaling molecules (Fig. 6s-z). This model failed to capture the delay in the rate of nuclear Ca^{2+} increase to maximum in elliptical cells (Fig. 5h). This suggests that the model specification was incomplete and additional details may be needed to make the model more realistic[59]. Since cell shape determines nuclear shape, we hypothesized that as the cell elongates, invaginations in the nuclear membrane may decrease. As nuclear invaginations have been shown to be related to nuclear calcium dynamics[60-62], we introduced a calcium permeability term in the model, by introducing a second order reaction dependent on the nuclear permeability, NPC, using the same circular and elliptical geometries (Supplementary Fig. 12). NPC represents the net nuclear permeability which may be due to an increase in nuclear membrane surface area and/or increase in nuclear pores; if NPC=0, the nuclear membrane is completely impermeable to cytoplasmic Ca^{2+}; if NPC=1, the nuclear membrane is completely permeable to the cytoplasmic Ca^{2+} and mirrors the cytoplasmic Ca^{2+} transient. When nuclear permeability in circular cells was three times higher compared to elliptical cells, there was closer agreement between the model and experimental temporal behavior in both cytoplasmic and nuclear Ca^{2+} (Supplementary Fig. 13), suggesting that nuclear membrane of elliptical cells are less permeable to cytoplasmic Ca^{2+}, compared to circular cells. The net effect of decreased nuclear permeability led to higher integrated nuclear Ca^{2+} signals in cells, which increases its availability for slower downstream processes in the nucleus that are driven by Ca^{2+} [25, 26]. Thus the whole-cell model, coupled with organelle location based on curvature, captures key findings of Ca^{2+} dynamics in VSMC of different shapes.

DISCUSSION

One of the key features of intracellular signal flow is the spatial organization of information propagation. This feature is used in multiple cell types to closely regulate the temporal dynamics of second messengers such as calcium and cAMP. For example, in cardiac and skeletal muscle cells, T-tubules, which are tubular invaginations that penetrate into the center of the cell are enriched in L-type calcium channels[63, 64] . Mature dendritic spines in neurons have a specialized ER called the spine apparatus, which is thought to play a role in regulating calcium concentrations in spines[65]. Here, we bring together several seemingly independent effects due to change in global cell shape to provide an integrated view of how curvature, affects organelle location as well as distribution of receptors in the plane of the membrane to modulate signal transduction and thus affect cellular function (Fig. 7). Shape and biochemical signaling are coupled together in a feedback loop to maintain phenotype: cell shape integrates external mechanical and chemical signals on the plasma membrane[3, 4] while intracellular signaling cascades containing chemical information in the form of reaction kinetics, in turn regulate cell shape[66, 67]. We propose that shape-dependent endomembrane and nuclear organization serves as the critical link that connect these two components in the feedback loop. This intricate, non-

linear coupling of geometric and chemical information can potentially lead to signal amplification to control phenotype.

We used VSMC as a model system to unravel the complex relationship between global cell curvature, signaling, and endomembrane organization. During atherogenesis, disruption of local microenvironment in the medial layer of blood vessels causes VSMC to lose its native spindle shape, and subsequently lose contractile function[24, 68]. It was not clear how loss of shape can to a decrease in contractile function. This study provides a mechanistic explanation for the functional role of shape in VSMC contractile function. Cell shape governs membrane curvature, which enables the emergence of systems level properties; cell elongation simultaneously concentrates plasma membrane receptors in the flatter regions of the membrane and reduces the distance between the PM-SR and SR-nucleus in the same region, hence effectively forming a diffusion-restricted domain where receptors, SR and the nucleus become closer to each other, establishing high effective IP_3 and Ca^{2+} concentration in the cell center. Given the slow diffusion coefficient of IP_3 ($\leq$ 10 $\mu m^2/s$) which limits the range of action over which it can exert its signal[69] and the dimensions of typical spindle-shaped VSMC (long axis $\geq$150 µm and short axis length of $\leq$ 10 µm), control of endomembrane organization by cell shape is a physical, non-genomic mechanism by which IP_3/Ca^{2+} signals can be locally amplified in order to achieve high concentration of Ca^{2+} globally. These can further regulate contractility and Ca^{2+}-dependent gene expression in the nucleus. Although the effect of cell shape on individual readouts of signaling may appear small, the collective and progressive amplification of signal transduction through coupled reaction kinetics and spatial organelle organization is sufficient to result in different regimes of phenotypic function.

While we have extensively explored the role of cell shape in signaling here and previously[3, 4], features that we have not considered here, such as the forces exerted by the extracellular microenvironment on the cell, and vice versa, also play a critical role in transmitting geometric information[70, 71], trafficking[72], and signal transduction[73]. Furthermore, the interaction between signaling and cytoskeletal remodeling can lead to changes in cell shape and local curvature[74, 75]. Our observations of increasing anisotropy and robustness in expression of actin myofibrils, along with increased nuclear SRF localization with aspect ratio indicate that cytoskeletal signaling also contributes towards the contractile phenotype of VSMC. Cytoskeletal and Ca^{2+} signaling may act in concert in maintaining the differentiated phenotype of spindle-shaped VSMC. We were able to uncover unique aspects of signal flow in cells based on geometry and chemical reaction cascades alone and coupling the role of cytoskeletal interactions is a focus of future studies. We conclude that being at the right place at the right time is critical for information to flow from one compartment to another and for short term signals like Ca^{2+} to have long lasting effects such as contractility and transcription factor activity.

METHODS

Cell culture. A10 cells, which are VSMC from thoracic/medial layer of rat aortas, were obtained from American Type Culture Collection (CRL-1476). A10 cells were maintained in Dulbecco's modified eagle's medium (DMEM, Gibco), supplemented with 10% Fetal Bovine Serum, 1% penicillin/streptomycin, at 37 °C and 5% CO_2. Cells were transfected using Neon Transfection System (Life Technologies) according to manufacturer's instructions. Briefly, 5 x 10^5 cells were electroporated with 1 µg DNA in suspension buffer, with the following electroporation settings: 1400 V, 2 pulses, 20 ms pulses each. Cells were then suspended in DMEM supplemented with 10% FBS and then allowed to adhere on 3D biochips. Forty-eight hours post-transfection, cells were imaged using Hanks Balanced Salt Solution (HBSS) supplemented with $CaCl_2$, $MgCl_2$ and 10 mM HEPES.

Fabrication of 3D biochips. Patterned surfaces were fabricated by conventional photolithography using SU8 photoresist[76]. Briefly, cover glass slides were cleaned by sonication in isopropanol and deionized water for 15 minutes and baked at 110 °C overnight and photolithography was subsequently performed using standard vacuum hard-contact mode. Before plating of cells onto 3D biochips, microfabricated surfaces were washed with 50 µg/mL gentamicin and then incubated with 0.5% Pluronic for at least 3 hours. The 3D biochips were then washed with PBS and were seeded with cells.

Immunofluorescence of cells in 3D biochips. Cells were seeded onto the 3D biochips and were allowed to adhere and comply with the patterns for at least 24 hours. After assay treatments, cells were fixed with 4% paraformaldehyde (Electron Microscopy) for 15 minutes at room temperature, washed with PBS, permeabilized with 0.2% saponin for 30 minutes and blocked with 4% normal goat serum doped with 0.05% saponin for 1 hour. Cells were then incubated overnight with primary antibodies (sources and catalog numbers shown in table below) that had been diluted in blocking solution at 4 °C. Cells were washed with PBS and samples were incubated with secondary antibodies (Alexa 488, Alexa 568 and/or Alexa 647) for 1 hour at room temperature. For organelle staining, cells were counter-stained with Actin Green and DAPI counterstains in addition to the secondary antibodies. Cells were then imaged on a Zeiss LSM 880 microscope equipped with 60x objective. Same acquisition settings were applied across different conditions that were compared (laser power, gain settings, magnification, zoom, pixel size and slice thickness). For quantitative immunofluorescence of M_3R, a Z-stack of 30-40 slices using a slice thickness of 0.5 µm were obtained for each cell. Z-stack datasets were then pared down to 21-22 slices encompassing the entire height of the cell (mean cell height ~ 10 µm). Alignment, registration and cropping were performed to ensure each image had the same x-y dimensions (circular cells = 253 x 246 pixels, elliptical cells (AR 1:10) = 106 x 512 pixels). Per condition, images of cells obtained from the same z-plane (3.0 µm from the confocal slice corresponding to the bottom region of the plasma membrane), were averaged to obtain the averaged distribution of M_3R in different regions of the cell. For immunofluorescence of transcription factors, multi-channel images consisting of DAPI, Actin Green (Invitrogen), and primary antibodies for NFAT, SRF or myocardin were aligned and stitched using the ZEN 2014 software. Image analysis and quantification was performed using ImageJ scripts. Briefly, nuclei were segmented in the DAPI channel. Corresponding cytosol and whole cell objects were outlined utilizing the contrast enhanced phalloidin channel to define cell boundaries. Nuclear-to-cytoplasmic transcription factor ratio was defined as the ratio of the mean transcription factor

intensity colocalizing with the nuclear object divided by the mean intensity of the corresponding cytosol object. All measurements were exported directly to csv files and were subsequently analyzed using MATLAB to generate plots.

Antibody	Dilution	Source
Calnexin	IF 1:100	Abcam, cat # ab22595
Protein Disulfide Isomerase (PDI) (C81H6)	IF 1:100	Cell Signaling, cat # 3501
Nogo-A/Reticulon-4	IF 1:100	Cell Signaling, cat # ab47085
α-tubulin	IF 1:100	Cell Signaling, cat # 2144
AIF mitochondrial marker (D39D2)	IF 1:100	Cell Signaling, cat # 5318
EEA1 – Early endosome marker (C45B10)	IF 1:100	Cell Signaling, cat # 3288
RCAS1 (D2B6N) Golgi marker	IF 1:100	Cell Signaling, cat # 9091
Muscarinic Acetylcholine Receptor 3 (M_3R)	IF 1:100	Abcam, cat # ab126168
NFATc1 antibody	IF 1:100	Abcam, cat # ab2722
SRF antibody	IF 1:100	Cell Signaling, cat # 4261
Myocardin	IF 1:100	Abcam, cat # 22073

Airy-scan Imaging of Live Cells. VSMC conforming in the 3D biochips were simultaneously labeled with 1 µM CellMask Plasma Membrane tracker (Life Technologies), 1 µM CellMask ER marker (BODIPY TR Glibenclamide), in HBSS buffer supplemented with 1% Pyruvate, 1% HEPES and 1 mM Trolox, for 5 minutes at room temperature. Images were acquired using Zeiss LSM 880 using Airy-scan imaging equipped with 63x 1.4 Plan-Apochromat Oil objective lens at 30 ºC. Z-stacks using with an interval of 0.15 µm were collected for the entire cell height which approximated 10-12 µm. Z-stack analyses and other post-acquisition processing were performed on ZEN software (Carl Zeiss).

Calcium Measurements. VSMC were seeded on 3D biochips. Calcium measurements in 3D biochips were performed as previously described with modifications[77]. Briefly, cells in 3D biochips were serum-starved for 12 hours and loaded with 5 µM of calcium green (dissolved in DMSO) for 30 minutes at room temperature, with Hanks Balanced Salt solution, (HBSS) supplemented with $CaCl_2$, $MgCl_2$ and 10 mM HEPES. Calcium Green was imaged using Zeiss 510 equipped with 40x Apochromat objective at acquisition frame rate of 4 fps (250 ms acquisition time), and Calcium Green was excited using Argon ion laser 488 at low transmittivity (1%) to prevent photobleaching. Image stacks acquired were then imported into Fiji/ImageJ. Background subtraction were performed on the time stacks by using a rolling ball radius of 50 pixels. Cytoplasm and nuclear regions of interest (ROI) were chosen by performing a maximum intensity projection of the time-stack and specifying a 5 µm radius circle within the the nuclear and cytoplasmic regions. To convert intensity values to Ca^{2+} concentration, modified Grynkiewicz equation was used, defined as: [Calcium] = $K_D[\frac{(F-Fmin)}{(Fmax-F)}]$. Where F_{min} is the average fluorescence intensity of the ROI after addition of 100 µM BAPTA AM, F_{max} is the average fluorescence intensity of the ROI after addition of 0.100 µM A23187. Integrated Ca^{2+} were obtained using the trapz() function in MATLAB.

FRET imaging. MLCK-FRET plasmid is a kind gift from Dr. James T. Stull (University of Texas Southwestern Medical Center). The MLCK-FRET plasmid is a calmodulin-binding based sensor where calmodulin binding sequence is flanked with eCFP and eYFP and exhibits decreased FRET upon binding with calmodulin[52,18]. Cells expressing MLCK-FRET were imaged

using Zeiss LSM 880 (Carl Zeiss, Jena, Germany), at 37 ºC incubator, fitted with Plan-Apochromat 20x, equipped with 458 nm and 514 nm Argon ion laser lines for excitation of eCFP and eYFP respectively. Incident excitation light was split using an MBS 458 nm/514 nm beam splitter and collected on a 32-spectral array GaAsp detector. The fluorescence emission was collected from 463-520 nm (ECFP), 544-620 nm (FRET channel and eYFP channel). Intensity based ratiometric FRET were obtained using custom-written scripts in ImageJ and MATLAB. Since MLCK-FRET is a single-chain construct, decrease in FRET, and increase in MLCK binding to calmodulin, was expressed as the ratio of emission intensity at 520 nm/emission intensity at 510 nm normalized at the basal levels.

NFAT imaging. HA-NFAT1(4-460)-GFP was a gift from Anjana Rao (Addgene plasmid # 11107). Patterned cells expressing NFAT-GFP was imaged using Zeiss 880, using Argon ion laser 488 nm, as described above and 1.4 NA objective, with an acquisition rate of 1 frame every 10 seconds. Time series image stacks were analyzed using ImageJ. Regions of interest of identical size were drawn in the cytoplasmic and nuclear regions of interest and the ratios of these intensities were computed over time.

Electron Microscopy. 3D biochips containing fixed A10 cells were embedded in Embed 812 resin (Electron Microscopy Sciences (EMS), Hatfield, PA) using the following protocol. Cells were rinsed in 200mM phosphate buffer (PB), osmicated with 1% osmium tetroxide/PB, washed with distilled water (dH20), and *en bloc* stained with aqueous 2% uranyl acetate, washed with dH2O and dehydrated via increasing ethanol (ETOH) series /distilled water (25%, 60%, 75%, 95% and 100% ETOH). Cells were further dehydrated using propylene oxide (PO), and embedded using ascending PO:EPON resin concentrations (2:1, 1:1, 1:2, pure). Prior to solidification, the coverslips were placed on 1”X 3” microscope slides, and multiple open ended embedding capsule with a 1 × 1 cm face (EMS) were placed on the coverslips covering the areas of interest. The resin was then polymerized in a vacuum oven at of 65 °C for 8–12 hours. After the first layer was solidified, the capsule was topped off with more resin and put back in the oven for another 8–12 hours. Capsules containing cells within 3D biochips were removed from coverslips using previously described methods[78]. Briefly, to separate the block from the coverslip, a hot plate was heated to 60°C and the microscope slide was placed directly on a pre-heated hot plate for exactly 3 minutes and 30 seconds. The slide was removed from the hot plate and the capsules carefully dislodged free from the coverslips. Once separated, the block face retains the cells within the 3D biochips. The block was coarsely trimmed with a double-edged razorblade, and a Diatome cryotrim 45° mesa-trimming knife (EMS) was used to finely trim the block. Using as large a block face as possible, 70 nm ultrathin sections were cut from the block surface using an ultra-thin diamond knife (EMS), and a Leica EM UC7 ultramicrotome (Buffalo Grove, IL). All sections coming off the block face were collected. Sections were collected using a Perfect Loop (EMS) and transferred to a 2 × 1 mm formvar-carbon coated reinforced slot grid (EMS). The sample was dried on the grid and transferred to Hiraoka Staining Mats (EMS) for heavy metal staining. Grids were stained with 3% uranyl acetate in water for 40 minutes, washed and stained with Reynold’s lead citrate for 3 minutes, washed and allowed to dry. Electron microscopy images were taken using a Hitachi 7000 Electron Microscope (Hitachi High Technologies America, Inc.) equipped with an AMT Advantage CCD camera. Cells were viewed at low-magnification to identify areas of interest (cell tip versus cell body) before high magnification imaging. Images were transferred to Adobe Photoshop CS3 (version 10), and adjusted for brightness and contrast. Measurement of plasma membrane to ER distances from

electron microscopy images were performed blindly. Briefly, sample information from images were removed and images were saved with a randomized filename. Image contrast was further enhanced using ImageJ using contrast-limited adaptive histogram equalization (CLAHE). Only images with discernible smooth ER closely apposed to the plasma membrane were analyzed and distances were measured at optimal xy orientations at 50 nm intervals using ImageJ. Data was graphed using Excel and MATLAB.

Statistics. Results are presented as mean $\pm$ standard error of the mean from at least three independent experiments. Normality was determined using Shapiro-Wilk test using a p-value $\geq$ 0.05. If distribution is normal, a two-tailed Student's t-test was performed. For datasets with non-normal distribution, two-tailed Mann-Whitney test was used. $P < 0.05$ was considered statistically significant.

Model Development. We formulated a phenomenological model to study the role of PM-SR distances. The complete derivation and mathematical solution is given in the Supplementary Information. Complete details of the simulations using finite-element methods in COMSOL and using finite-volume methods in *Virtual Cell* are given in the Supplementary Information.

Data Availability. Data supporting the findings of this study are available within the paper and its supplementary information.

ACKNOWLEDGEMENTS

We thank Dr. Eric Sobie, Dr. Marc Birtwistle, Dr. Evren Azeloglu, Miriam Bell and Michael Getz for discussion and reagents. This work was supported NIH Grants GM072853 and the Systems Biology Center grant P50GM071558. RC was supported by a NIH postdoctoral fellowship F32GM116415 and research in PR's laboratory is supported by ARO W911NF-16-1-0411, AFOSR FA9550-15-1-0124, and NSF PHY-1505017.

Figure 1

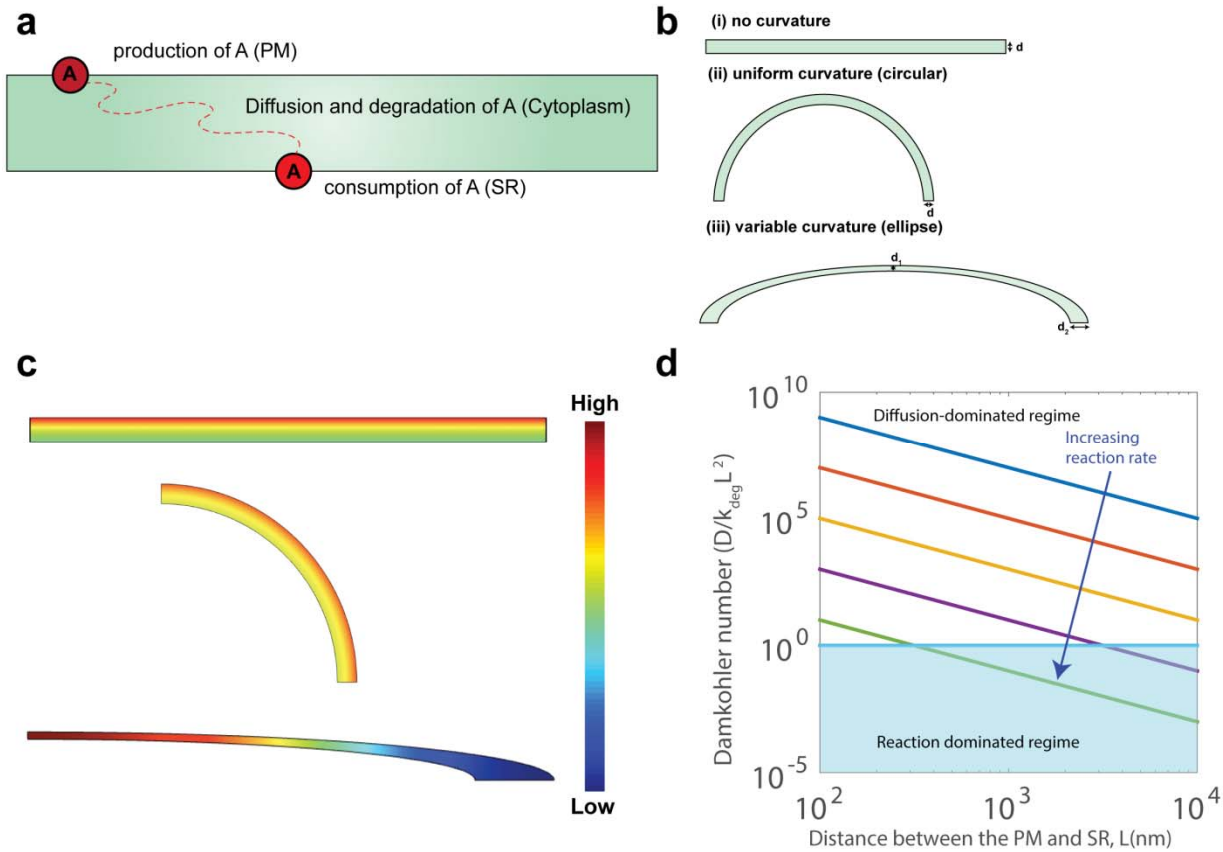

Figure 1 Phenomenological model describing the dynamics of a signaling molecule produced at a membrane and consumed at an organelle membrane compartment as a function of curvature. (a) Dynamics of a signaling molecule can be described by its production, diffusion, and degradation in the cytoplasmic space and consumption at an intracellular organelle membrane. (b) Three different geometries were used to test how curvature of the membrane and distance between the plasma membrane (PM) and the inner membrane, a sarcoplasmic reticulum (SR) in this case, affect the spatio-temporal dynamics of the signaling molecule 'A'. (c) Reaction-diffusion modeling predicts that curvature and distance between the PM and SR will both affect the spatial distribution of A. (d) The Damkohler number for different values of PM-SR distance, 'd', and rate of degradation. 'k_{deg}'. For physiological distances, the dynamics of A are dominated by diffusion.

Figure 2

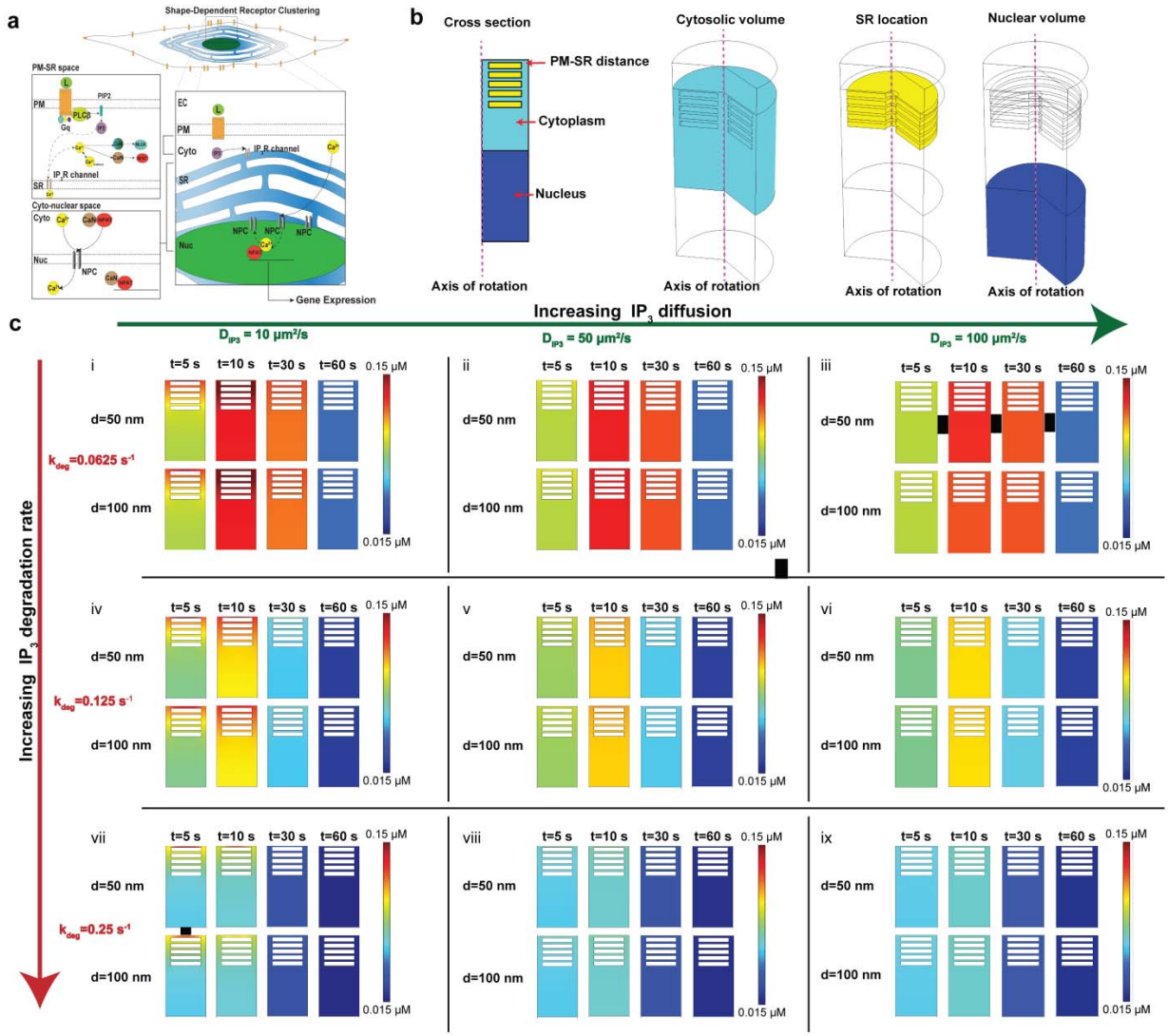

Figure 2. Small length scale simulations show a critical relationship between IP_3 and PM-SR distance (a) Biochemical events that govern Ca^{2+} signaling in VSMC including GPCR-$G_{\alpha q}$ cycling on the membrane, PLCβ activation, IP_3 production and IP_3R-mediated Ca^{2+} release from SR. b) Cross-section and geometries representing different compartments governing biochemical events. We model a small part of the cell as a cylinder. The cytosolic volume is shown in cyan, the SR modeled as cylindrical disks shown in yellow and the nucleus is shown in blue and the axis of symmetry is shown in pink. c) Effect of IP_3 diffusion and degradation rate are shown for two different distances between the PM and the SR. Panels (i-iii) show the effect of increasing IP_3 diffusion ((i) 10 $\mu m^2.s^{-1}$, (ii) 50 $\mu m^2.s^{-1}$, and (iii) 100 $\mu m^2.s^{-1}$) on IP_3 concentration at 5s, 10s, 30s, and 60s for a degradation rate k_{deg}= 0.0625 s^{-1} for two different values of d (50 nm and 100 nm). Panels (iv-vi) show similar calculations for k_{deg} =0.125 s^{-1} and panels (vii-ix) for k_{deg}=0.25 s^{-1}.

Figure 3

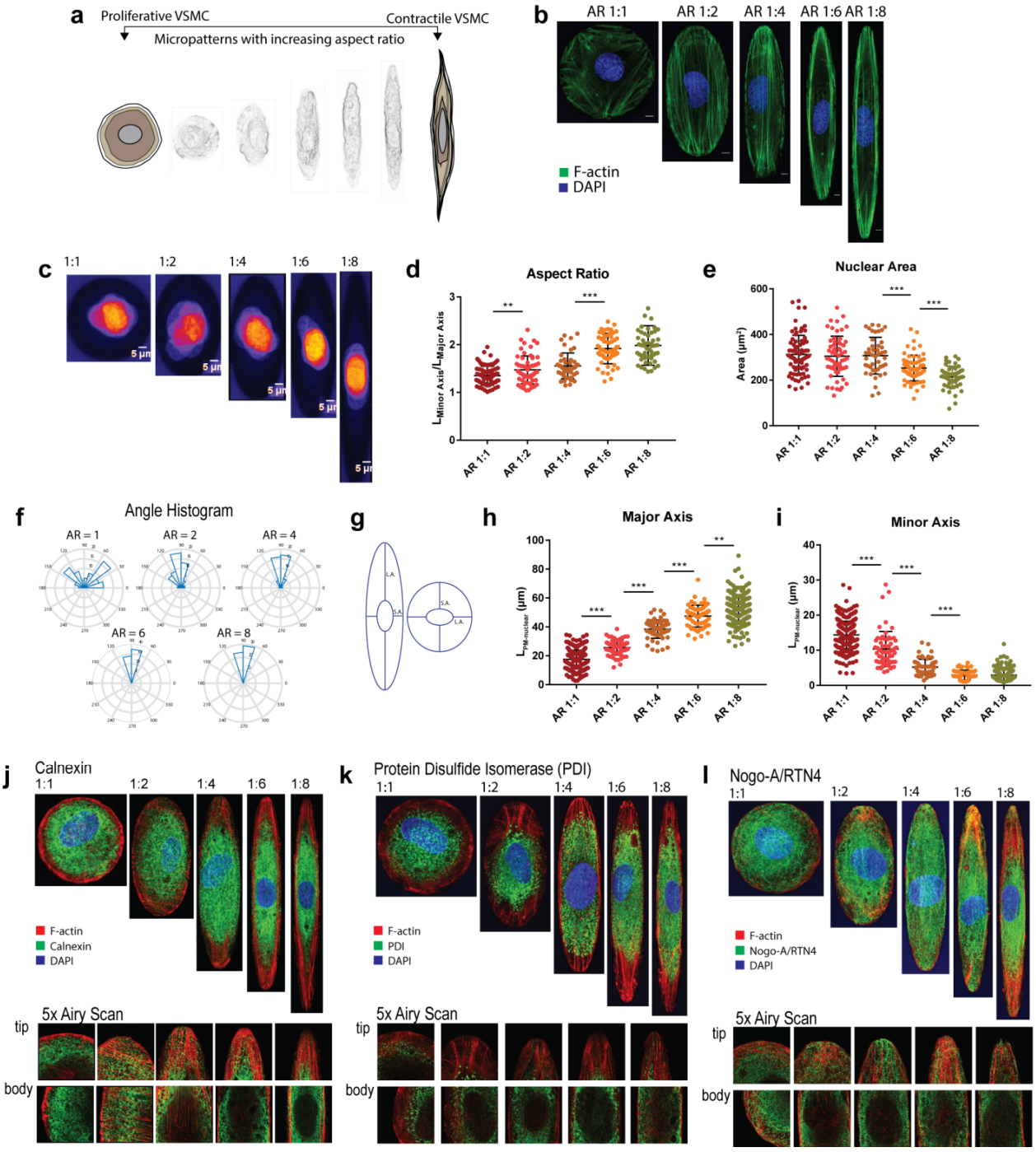
a
Proliferative VSMC
Contractile VSMC
Micropatterns with increasing aspect ratio
b
AR 1:1
AR 1:2
AR 1:4
AR 1:6
AR 1:8
F-actin
DAPI
c
1:1
1:2
1:4
1:6
1:8
5 µm
d
Aspect Ratio
L_Minor Axis/L_Major Axis
AR 1:1
AR 1:2
AR 1:4
AR 1:6
AR 1:8
e
Nuclear Area
Area (µm²)
f
Angle Histogram
AR = 1
AR = 2
AR = 4
AR = 6
AR = 8
g
L.A.
S.A.
h
Major Axis
L_PM-nuclear (µm)
i
Minor Axis
j
Calnexin
F-actin
Calnexin
DAPI
5x Airy Scan
tip
body
k
Protein Disulfide Isomerase (PDI)
F-actin
PDI
DAPI
l
Nogo-A/RTN4
F-actin
Nogo-A/RTN4
DAPI

Figure 3 Cell shape impacts cytoskeletal organization and organelle location. Whole cell shape changes location and distribution of subcellular organelles in a systematic manner. (a) Biomimetic, microfabricated surfaces with graded aspect ratios fine-tune the shape of VSMC and its enclosed organelles. (b) Actin organization is dependent on cell shape. (c) Cell shape affects nuclear shape, size and distance to PM. Representative images of VSMC compliant in patterns with increasing AR stained for DAPI. Scatterplots of whole aspect ratio versus (d) nuclear aspect ratio (e) size (area μm^2) (f) orientation with respect to the major axis of the cell ($N_{AR1:1}=82$, $N_{AR1:2}=60$, $N_{AR1:4}=45$, $N_{AR1:6}=65$, $N_{AR1:8}=54$). (g) Relationship between whole cell shape and PM-nuclear distance was determined by segmenting cell and nuclear boundaries with Actin Green and DAPI respectively. Distances between nuclear and plasma membrane boundaries were measured along the long and short axes of the nucleus. (h) Increasing the cellular aspect ratio increases the distance between the nucleus and the plasma membrane in the major axis of the cell while (i) decreasing the PM-nuclear distance in the minor axis of the cell (**$P \leq 0.05$, ***$P \leq 0.0001$, two-tailed t-test). (j-l) SR distribution in VSMC seeded in AR 1:1 to 1:8 staining for SR membrane markers (panels below show 5x magnified Airy scan images of tip and body of images shown) (j) calnexin (k) protein disulfide isomerase (PDI) and (l) reticulon-4.

Figure 4

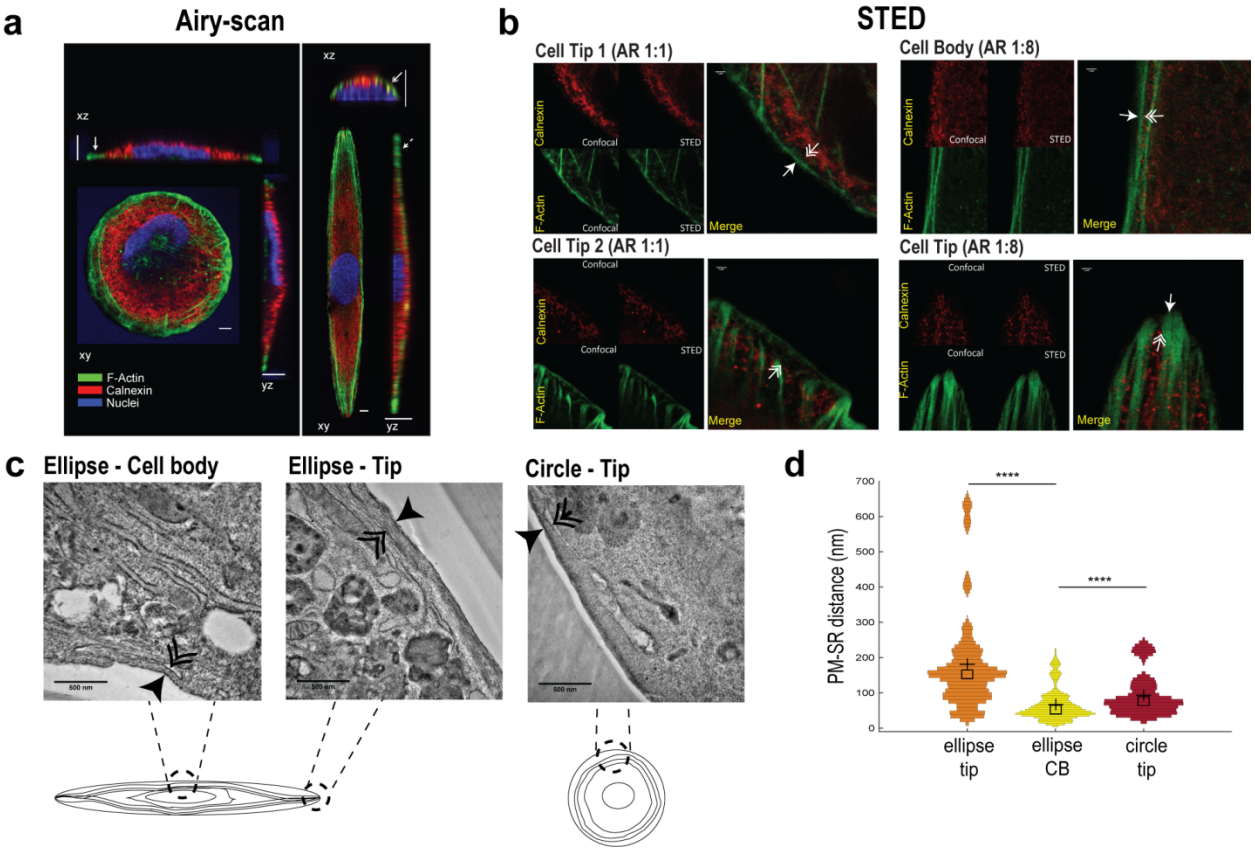

Figure 4 Shape impacts PM-SR distances in 3D. a) (Left panel) 3D confocal volume scans of VSMC cultured in circle and ellipse (Aspect ratio of 1:8) patterns showing F-Actin (green), ER membrane marker calnexin (red) and nuclei (blue). Increased co-localization of red and green pixels are seen in the xz (short axis) cross-section of elliptical cells (solid double arrow heads), while little co-localization is evident in tips of both circular and elliptical cells (solid single-arrow heads and dashed single-arrow heads, respectively). (Right panel) Super-resolution STED imaging of F-actin (green), calnexin (red), in cell tips of circular cells (AR 1:1) and in cell tip and cell body of elliptical cells (AR 1:8). b) Representative TEM micrographs sampled from corresponding regions in micropatterned cells (cartoon). Single-headed arrows indicate the plasma membrane and double-arrows indicate smooth, peripheral SR, apposed to the plasma membrane. (c) Distribution plots of PM-SR distances obtained from TEM images, mean and median are shown as crosses and squares respectively. ($N_{ellipse\ tip}$=329, $N_{cell\ body}$ = 254, $N_{circle\ tip}$ = 115, ****P < 0.0001, two-tailed Mann-Whitney test).

Figure 5

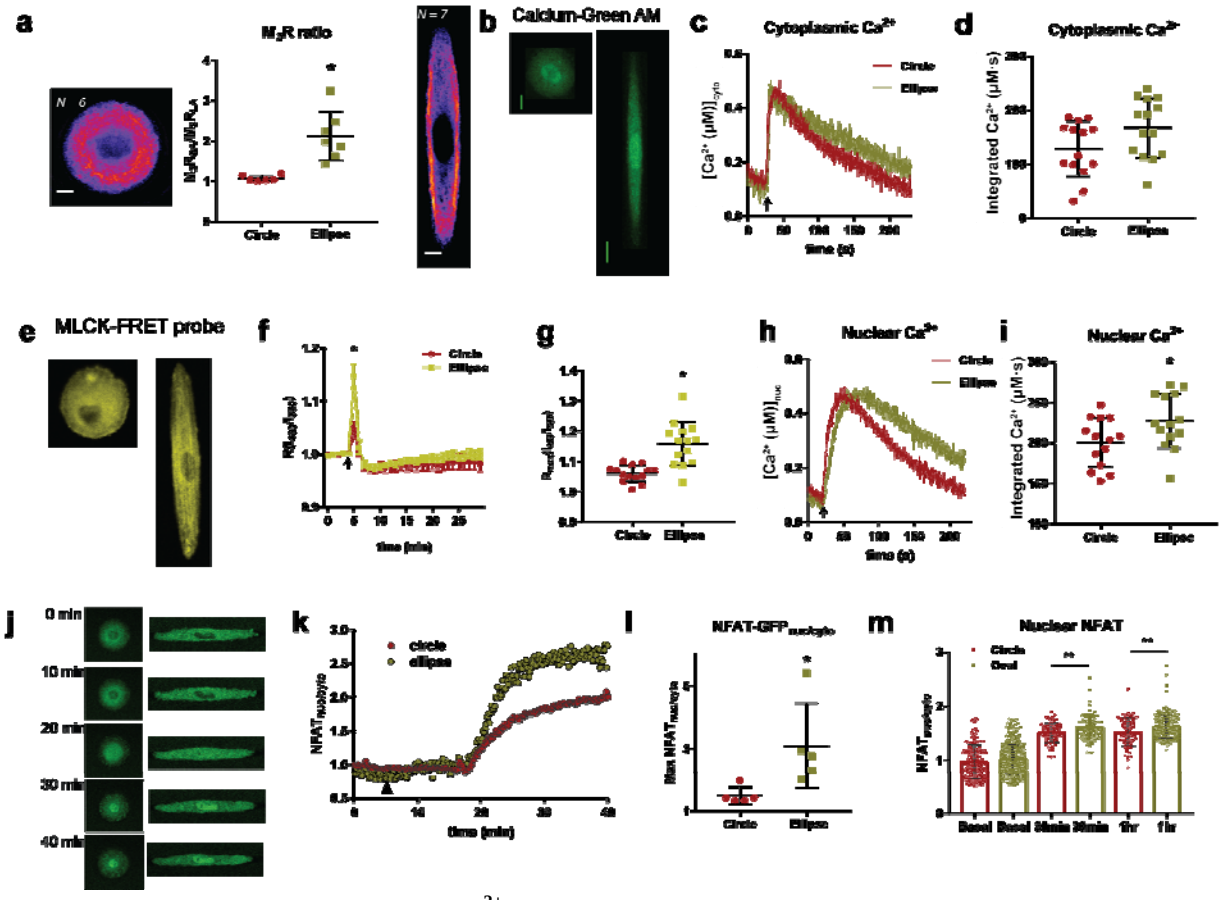

Figure 5. Shape impacts $M_3R/IP_3/Ca^{2+}$/NFAT signaling in VSMC. (a) Average intensity of M_3R along the length of the cell in circular (*N=6)* and oval *(N=7)* VSMC. Differences in anisotropic distribution of M_3R were quantified by obtaining the ratio of M_3R staining intensities on the short and long axes (M_3R_{SA}/M_3R_{LA}, mean$\pm$SEM ellipse=2.1 $\pm$ 0.6 A.U. *N = 7*, circle= 1.1 $\pm$ 0.1 A.U., *N=6*, *P=0.0016, two-tailed t-test). (b) Circular and elliptical cells were loaded with Calcium-Green AM dye, to measure Ca^{2+} signaling in response to 10 μM carbachol (c) average time-course of cytoplasmic Ca^{2+} in response to CCh (circle, N=14, oval, N=14, stimulated at arrow indicated) (d) Scatterplot of cytoplasmic integrated Ca^{2+} (area-under-the-curve) per cell in circular and elliptical cells. (e) Circle and elliptical cells expressing MLCK-FRET probe (f) temporal MLCK activation in circular and ellipse VSMC upon stimulation with carbachol, activation was measured by decrease in FRET and increase in R480/520 (g) scatterplot of maximal $R(I_{480}/I_{520})$ from individual cells expressing MLCK-FRET probe. (*P$\leq$0.0001, two-tailed Mann Whitney test). (h) average time-course of nuclear Ca^{2+} in response to CCh (i) scatterplot of nuclear integrated Ca^{2+} (area-under-the-curve) in circular and elliptical VSMC. (*P = 0.035, two-tailed t-test).(j) Representative VSMC complying to circle and elliptical micropatterns expressing NFAT-GFP, in basal and after stimulation with carbachol (k) Representative NFAT-GFP time-course (l) scatterplot of maximal $NFAT_{nuc/cyt}$ ratio in circle and elliptical cells Max $NFAT^{circle}_{nuc/cyto}$=1.51$\pm$0.12, *N=5*, Max $NFAT^{ellipse}_{nuc/cyto}$=3.10$\pm$0.60, *N=5*, p-value=0.0325, two-tailed t-test (*P = 0.0325, two-tailed t-test, N=5 for each group). (m) Single cell quantification of endogenous NFAT translocation ($NFAT_{nuc/cyt}$) in basal and M_3R stimulated states, in circle and ellipse VSMC. Bar plots shown are mean$\pm$SD with corresponding dot plot overlays (at basal, $N_{circle}=138$, $N_{ellipse}=284$, at time = 30 minutes, $N_{circle}=72$, $N_{oval}=81$, **P = 0.024, at time = 1 hour, $N_{circle}=69$, $N_{oval}=193$, **P = 0.010, two-tailed Mann-Whitney test). Scalebar, 10 μm.

Figure 6a-h

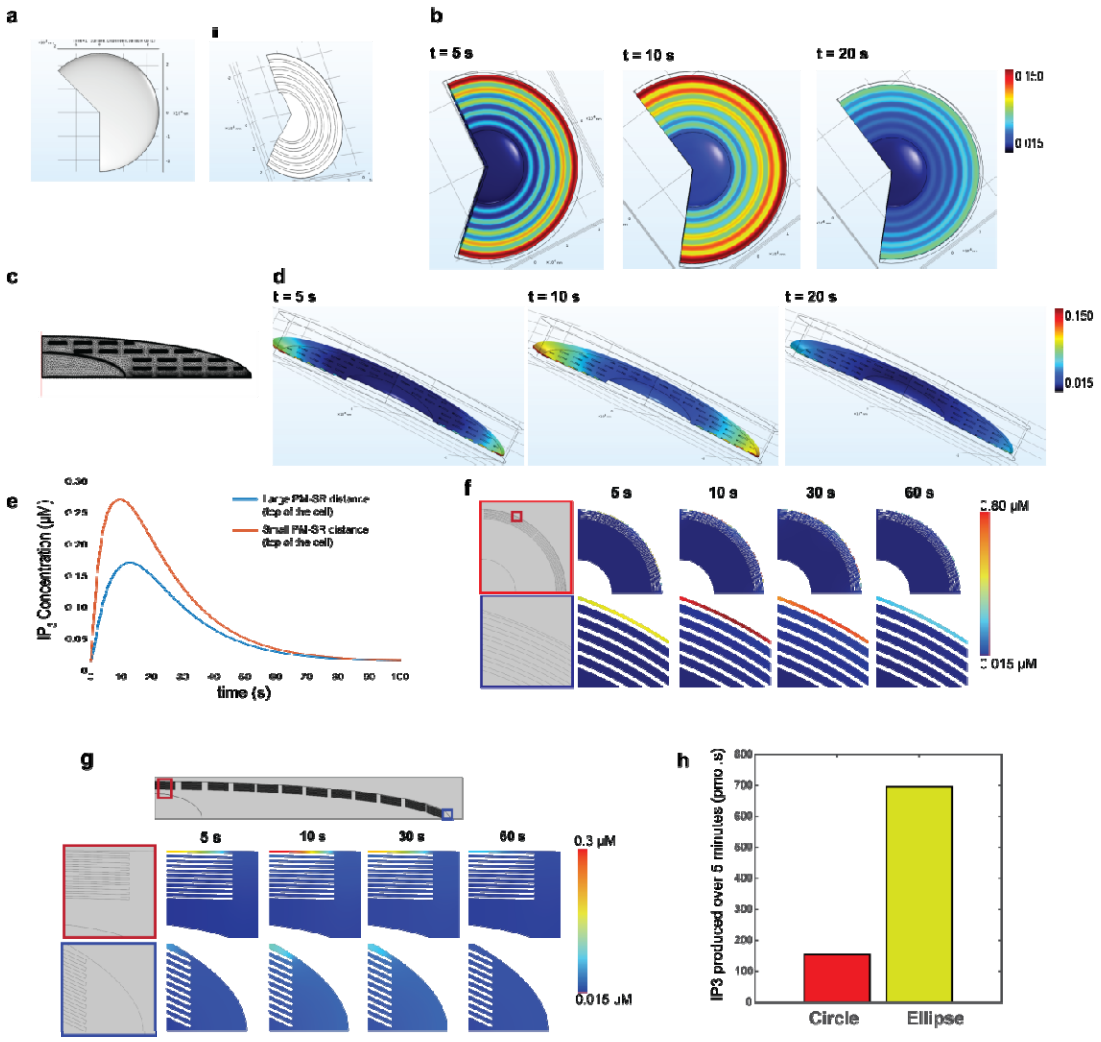

Figure 6(a-h). 3D spatial models provide mechanistic understanding of cell elongation-induced Ca^{2+} potentiation. 3D simulations show the effect of cell elongation on inter-organelle distances on IP_3/Ca^{2+} potentiation using COMSOL a) 3D geometry to represent a cell with a circular 2D cross section and the ER as tori placed at different distances from the PM with the finite element mesh. b) IP_3 spatial dynamics at 5, 10, and 20s in the geometry shown in panel a. c) 3D geometry to represent a cell with an elliptical cross section with rings of ER. d) IP_3 spatial dynamics at 5, 10, and 20 s in the ellipsoidal geometry. e) IP_3 dynamics at two different points near and far from the PM showing the PM-SR distance affects IP_3 transience. f –h) IP_3 concentrations in 2D circular geometries (f) and 2D elliptical geometries (g). h) IP_3 concentrations over space (the entire domain) and time were integrated, since integration of signal over time provides a buffer for time scale and damps out the effect of temporal fluctuations and spatial integration allows for conversion from concentration (moles per unit volume) to amount (moles). Shown are graphs comparing integrated IP_3 in circular and elliptical geometries.

Figure 6i-z

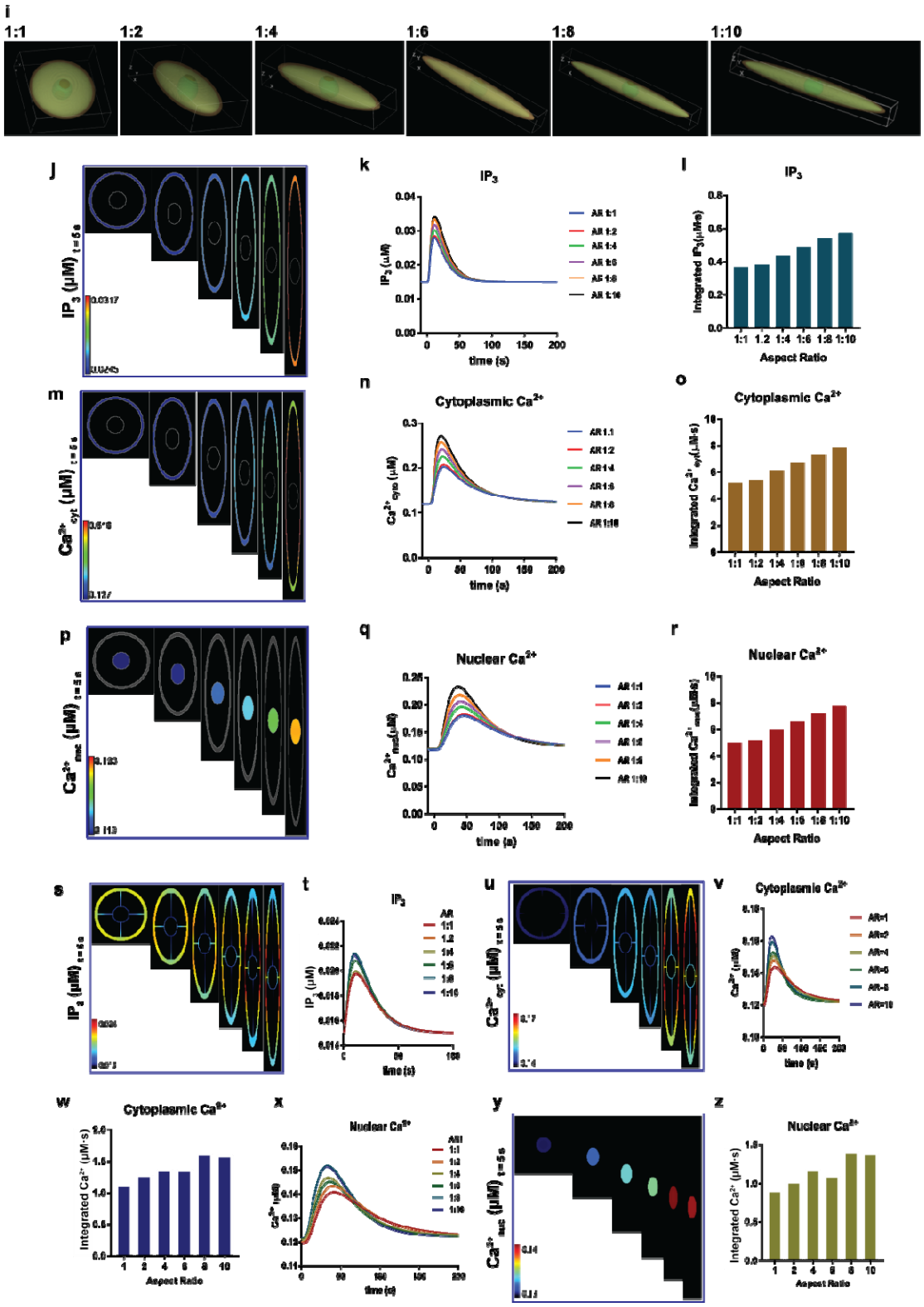
i
1:1
1:2
1:4
1:6
1:8
1:10
j
k
IP3
time (s)
l
IP3
Integrated IP3 (μM·s)
Aspect Ratio
m
n
Cytoplasmic Ca2+
time (s)
o
Cytoplasmic Ca2+
Aspect Ratio
p
q
Nuclear Ca2+
time (s)
r
Nuclear Ca2+
Aspect Ratio
s
t
IP3
time (s)
u
v
Cytoplasmic Ca2+
time (s)
w
Cytoplasmic Ca2+
Integrated Ca2+ (μM·s)
Aspect Ratio
x
Nuclear Ca2+
time (s)
y
z
Nuclear Ca2+
Integrated Ca2+ (μM·s)
Aspect Ratio

Figure 6i-z. 3D spatio-temporal PDE model of IP_3 and Ca^{2+} using *VCell.* i) 3D geometries of cells with constant volume and increasing surface area to volume ratio representing plasma membrane, SR membrane and nucleus in increasing elliptical aspect ratios. Global gradients, temporal dynamics and integrated concentration of IP_3 (j-l), cytoplasmic Ca^{2+} (m-o) and nuclear Ca^{2+} (p-r), exhibit progressively steeper gradients, and increased peak IP_3/$Ca_{cyt}{}^{2+}$/ $Ca_{nuc}{}^{2+}$with increasing cell aspect ratio, with the highest concentrations at the flatter regions of the cell (cell body). s-z) Corresponding 2D spatio-temporal PDE model of IP_3 and Ca^{2+} using 2D geometries show similar results to 3D simulations.

Figure 7

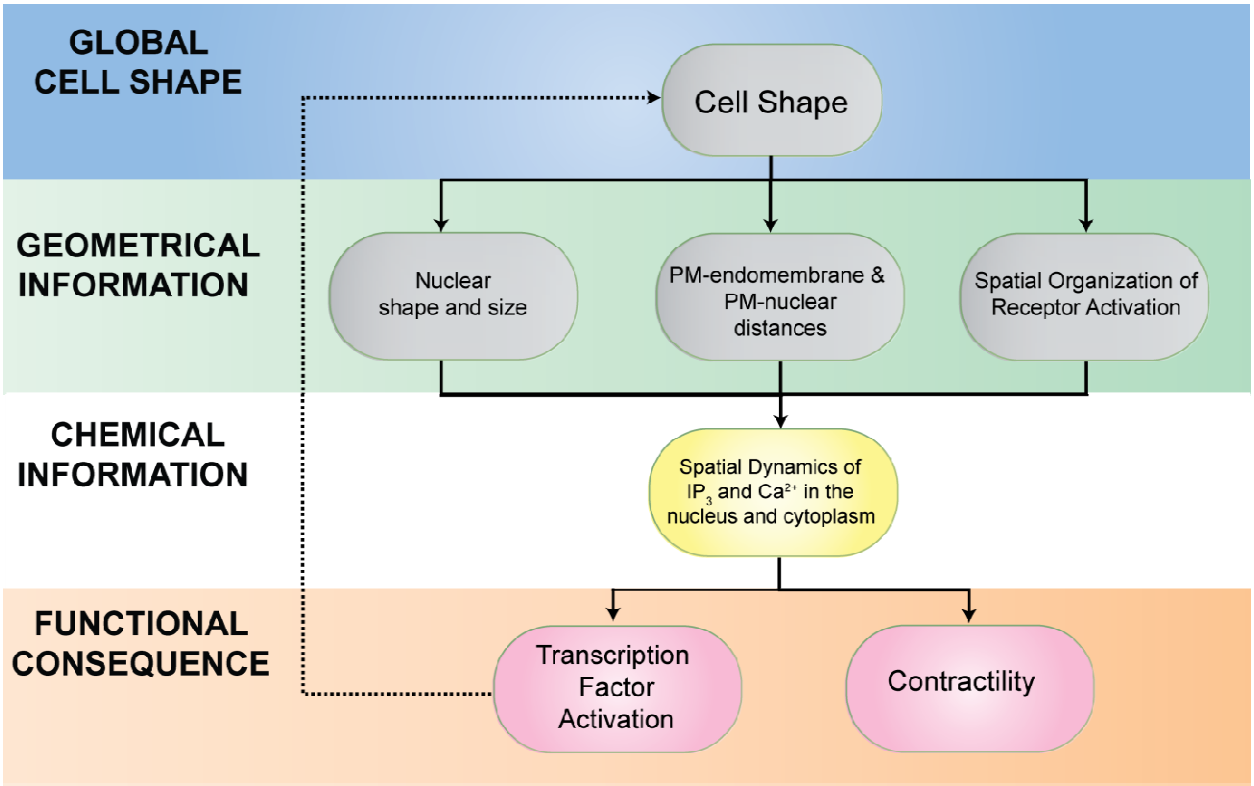

Figure 7. Systems approaches to controlling signaling through subcellular organization hierarchy. Physical determinants such as shape and geometrical information within the cell interact with organelle location and chemical information transfer to impact cellular function and gene expression, which in turn, feedback into cell shape. While each of these effects – shape, organelle location, and chemical information – may separately lead to small changes in signaling, collectively, these effects can lead to altered cellular function including transcription factor activation and contractility.

REFERENCES

1. Neves, S.R., Ram, P.T. & Iyengar, R. G protein pathways. *Science* **296**, 1636-1639 (2002).

2. Bhalla, U.S. & Iyengar, R. Emergent properties of networks of biological signaling pathways. *Science* **283**, 381-387 (1999).

3. Rangamani, P. *et al.* Decoding information in cell shape. *Cell* **154**, 1356-1369 (2013).

4. Neves, S.R. *et al.* Cell shape and negative links in regulatory motifs together control spatial information flow in signaling networks. *Cell* **133**, 666-680 (2008).

5. Meyers, J., Craig, J. & Odde, D.J. Potential for control of signaling pathways via cell size and shape. *Current biology* **16**, 1685-1693 (2006).

6. Kholodenko, B.N. Spatially distributed cell signalling. *FEBS letters* **583**, 4006-4012 (2009).

7. Vilardaga, J.-P., Jean-Alphonse, F.G. & Gardella, T.J. Endosomal generation of cAMP in GPCR signaling. *Nature chemical biology* **10**, 700-706 (2014).

8. Villaseñor, R., Nonaka, H., Del Conte-Zerial, P., Kalaidzidis, Y. & Zerial, M. Regulation of EGFR signal transduction by analogue-to-digital conversion in endosomes. *Elife* **4**, e06156 (2015).

9. Whitaker, M. Calcium at fertilization and in early development. *Physiological reviews* **86**, 25-88 (2006).

10. Pinton, P., Giorgi, C., Siviero, R., Zecchini, E. & Rizzuto, R. Calcium and apoptosis: ER-mitochondria Ca2+ transfer in the control of apoptosis. *Oncogene* **27**, 6407-6418 (2008).

11. Berridge, M.J. Calcium signalling and cell proliferation. *Bioessays* **17**, 491-500 (1995).

12. Wei, C. *et al.* Calcium flickers steer cell migration. *Nature* **457**, 901-905 (2009).

13. Berridge, M.J. & Taylor, C. in Cold Spring Harbor symposia on quantitative biology, Vol. 53 927-933 (Cold Spring Harbor Laboratory Press, 1988).

14. Hirose, K., Kadowaki, S., Tanabe, M., Takeshima, H. & Iino, M. Spatiotemporal dynamics of inositol 1, 4, 5-trisphosphate that underlies complex Ca2+ mobilization patterns. *Science* **284**, 1527-1530 (1999).

15. Berridge, M.J. Inositol trisphosphate and calcium signalling mechanisms. *Biochimica et Biophysica Acta (BBA)-Molecular Cell Research* **1793**, 933-940 (2009).

16. Brozovich, F.V. *et al.* Mechanisms of vascular smooth muscle contraction and the basis for pharmacologic treatment of smooth muscle disorders. *Pharmacological reviews* **68**, 476-532 (2016).

17. Kudryavtseva, O., Aalkjær, C. & Matchkov, V.V. Vascular smooth muscle cell phenotype is defined by Ca2+-dependent transcription factors. *FEBS journal* **280**, 5488-5499 (2013).

18. Hogan, P.G., Chen, L., Nardone, J. & Rao, A. Transcriptional regulation by calcium, calcineurin, and NFAT. *Genes & development* **17**, 2205-2232 (2003).

19. Miranti, C.K., Ginty, D.D., Huang, G., Chatila, T. & Greenberg, M.E. Calcium activates serum response factor-dependent transcription by a Ras-and Elk-1-independent mechanism that involves a Ca2+/calmodulin-dependent kinase. *Molecular and cellular biology* **15**, 3672-3684 (1995).

20. Wang, D.-Z. *et al.* Activation of cardiac gene expression by myocardin, a transcriptional cofactor for serum response factor. *Cell* **105**, 851-862 (2001).

21. Rensen, S., Doevendans, P. & Van Eys, G. Regulation and characteristics of vascular smooth muscle cell phenotypic diversity. *Netherlands Heart Journal* **15**, 100-108 (2007).

22. Rzucidlo, E.M., Martin, K.A. & Powell, R.J. Regulation of vascular smooth muscle cell differentiation. *Journal of vascular surgery* **45**, A25-A32 (2007).

23. Gomez, D. & Owens, G.K. Smooth muscle cell phenotypic switching in atherosclerosis. *Cardiovascular research*, cvs115 (2012).

24. Chamley-Campbell, J., Campbell, G.R. & Ross, R. The smooth muscle cell in culture. *Physiol rev* **59**, 1-61 (1979).

25. Owens, G.K., Kumar, M.S. & Wamhoff, B.R. Molecular regulation of vascular smooth muscle cell differentiation in development and disease. *Physiological reviews* **84**, 767-801 (2004).

26. Pitaval, A., Tseng, Q., Bornens, M. & Théry, M. Cell shape and contractility regulate ciliogenesis in cell cycle–arrested cells. *The Journal of cell biology* **191**, 303-312 (2010).

27. Alford, P.W., Nesmith, A.P., Seywerd, J.N., Grosberg, A. & Parker, K.K. Vascular smooth muscle contractility depends on cell shape. *Integrative Biology* **3**, 1063-1070 (2011).

28. Polte, T.R., Eichler, G.S., Wang, N. & Ingber, D.E. Extracellular matrix controls myosin light chain phosphorylation and cell contractility through modulation of cell shape and cytoskeletal prestress. *American Journal of Physiology-Cell Physiology* **286**, C518-C528 (2004).

29. Ron, A. *et al*. Cell shape information is transduced through tension-independent mechanisms. *Nature communications* **8**, 2145 (2017).

30. Eglen, R.M., Reddy, H., Watson, N. & Challiss, R.J. Muscarinic acetylcholine receptor subtypes in smooth muscle. *Trends in pharmacological sciences* **15**, 114-119 (1994).

31. Caulfield, M.P. Muscarinic receptors—characterization, coupling and function. *Pharmacology & therapeutics* **58**, 319-379 (1993).

32. Berridge, M.J. & Irvine, R.F. Inositol phosphates and cell signalling. *Nature* **341**, 197-205 (1989).

33. Bell, M., Bartol, T., Sejnowski, T. & Rangamani, P. Dendritic spine geometry and spine apparatus organization govern the spatiotemporal dynamics of calcium. *bioRxiv*, 386367 (2018).

34. Cugno, A., Bartol, T.M., Sejnowski, T.J., Iyengar, R. & Rangamani, P. Geometric principles of second messenger dynamics in dendritic spines. *bioRxiv* (2018).

35. Bird, R.B., Stewart, W.E. & Lightfoot, E.N. *Transport phenomena*. (John Wiley & Sons, 2007).

36. Pollard, T.D. & Cooper, J.A. Actin, a central player in cell shape and movement. *Science* **326**, 1208-1212 (2009).

37. McBeath, R., Pirone, D.M., Nelson, C.M., Bhadriraju, K. & Chen, C.S. Cell shape, cytoskeletal tension, and RhoA regulate stem cell lineage commitment. *Developmental cell* **6**, 483-495 (2004).

38. Vogel, V. & Sheetz, M. Local force and geometry sensing regulate cell functions. *Nature reviews Molecular cell biology* **7**, 265-275 (2006).

39. Storm, C., Pastore, J.J., MacKintosh, F.C., Lubensky, T.C. & Janmey, P.A. Nonlinear elasticity in biological gels. *Nature* **435**, 191-194 (2005).

40. Versaevel, M., Grevesse, T. & Gabriele, S. Spatial coordination between cell and nuclear shape within micropatterned endothelial cells. *Nature communications* **3**, 671 (2012).

41. Valm, A.M. *et al*. Applying systems-level spectral imaging and analysis to reveal the organelle interactome. *Nature* (2017).

42. Waterman-Storer, C.M. & Salmon, E.D. Endoplasmic reticulum membrane tubules are distributed by microtubules in living cells using three distinct mechanisms. *Current Biology* **8**, 798-807 (1998).

43. Wray, S. & Burdyga, T. Sarcoplasmic reticulum function in smooth muscle. *Physiological reviews* **90**, 113-178 (2010).

44. Wu, Y. *et al.* Contacts between the endoplasmic reticulum and other membranes in neurons. *Proceedings of the National Academy of Sciences*, 201701078 (2017).

45. Schauer, K. *et al*. Probabilistic density maps to study global endomembrane organization. *nAture methods* **7**, 560-566 (2010).

46. Ehlert, F.J. Contractile role of M 2 and M 3 muscarinic receptors in gastrointestinal, airway and urinary bladder smooth muscle. *Life sciences* **74**, 355-366 (2003).

47. Mundell, S.J. & Kelly, E. The effect of inhibitors of receptor internalization on the desensitization and resensitization of three Gs-coupled receptor responses. *British journal of pharmacology* **125**, 1594-1600 (1998).

48. Hansen, S.H., Sandvig, K. & Van Deurs, B. Clathrin and HA2 adaptors: effects of potassium depletion, hypertonic medium, and cytosol acidification. *The Journal of cell biology* **121**, 61-72 (1993).

49. Heuser, J.E. & Anderson, R. Hypertonic media inhibit receptor-mediated endocytosis by blocking clathrin-coated pit formation. *The Journal of cell biology* **108**, 389-400 (1989).

50. Toescu, E.C. & Verkhratsky, A. The importance of being subtle: small changes in calcium homeostasis control cognitive decline in normal aging. *Aging cell* **6**, 267-273 (2007).

51. Mizuno, Y. *et al.* Myosin light chain kinase activation and calcium sensitization in smooth muscle in vivo. *American Journal of Physiology-Cell Physiology* **295**, C358-C364 (2008).

52. Isotani, E. *et al.* Real-time evaluation of myosin light chain kinase activation in smooth muscle tissues from a transgenic calmodulin-biosensor mouse. *Proceedings of the National Academy of Sciences of the United States of America* **101**, 6279-6284 (2004).

53. George, J. *et al.* The contractile strength of vascular smooth muscle myocytes is shape dependent. *Integrative Biology* **6**, 152-163 (2014).

54. Crabtree, G.R. Calcium, calcineurin, and the control of transcription. *Journal of Biological Chemistry* **276**, 2313-2316 (2001).

55. Sotiropoulos, A., Gineitis, D., Copeland, J. & Treisman, R. Signal-regulated activation of serum response factor is mediated by changes in actin dynamics. *Cell* **98**, 159-169 (1999).

56. Liu, H.W. *et al.* The RhoA/Rho kinase pathway regulates nuclear localization of serum response factor. *American journal of respiratory cell and molecular biology* **29**, 39-47 (2003).

57. Creemers, E.E., Sutherland, L.B., Oh, J., Barbosa, A.C. & Olson, E.N. Coactivation of MEF2 by the SAP domain proteins myocardin and MASTR. *Molecular cell* **23**, 83-96 (2006).

58. Voeltz, G.K., Rolls, M.M. & Rapoport, T.A. Structural organization of the endoplasmic reticulum. *EMBO reports* **3**, 944-950 (2002).

59. Azeloglu, E.U. & Iyengar, R. Good practices for building dynamical models in systems biology. *Sci. Signal.* **8**, fs8-fs8 (2015).

60. Wittmann, M. *et al.* Synaptic activity induces dramatic changes in the geometry of the cell nucleus: interplay between nuclear structure, histone H3 phosphorylation, and nuclear calcium signaling. *Journal of Neuroscience* **29**, 14687-14700 (2009).

61. Queisser, G., Wiegert, S. & Bading, H. Structural dynamics of the cell nucleus. *Nucleus* **2**, 98-104 (2011).

62. Mauger, J.P. Role of the nuclear envelope in calcium signalling. *Biology of the Cell* **104**, 70-83 (2012).

63. Bers, D.M. Cardiac excitation–contraction coupling. *Nature* **415**, 198 (2002).

64. Scriven, D.R., Dan, P. & Moore, E.D. Distribution of proteins implicated in excitation-contraction coupling in rat ventricular myocytes. *Biophysical journal* **79**, 2682-2691 (2000).

65. Sala, C. & Segal, M. Dendritic spines: the locus of structural and functional plasticity. *Physiological reviews* **94**, 141-188 (2014).

66. Bakal, C., Aach, J., Church, G. & Perrimon, N. Quantitative morphological signatures define local signaling networks regulating cell morphology. *science* **316**, 1753-1756 (2007).

67. Sailem, H., Bousgouni, V., Cooper, S. & Bakal, C. Cross-talk between Rho and Rac GTPases drives deterministic exploration of cellular shape space and morphological heterogeneity. *Open biology* **4**, 130132 (2014).

68. Ross, R. Cell biology of atherosclerosis. *Annual review of physiology* **57**, 791-804 (1995).

69. Dickinson, G.D., Ellefsen, K.L., Dawson, S.P., Pearson, J.E. & Parker, I. Hindered cytoplasmic diffusion of inositol trisphosphate restricts its cellular range of action. *Sci. Signal*. **9**, ra108-ra108 (2016).

70. Mitra, A. *et al*. Cell geometry dictates TNFα-induced genome response. *Proceedings of the National Academy of Sciences* **114**, E3882-E3891 (2017).

71. Jain, N., Iyer, K.V., Kumar, A. & Shivashankar, G. Cell geometric constraints induce modular gene-expression patterns via redistribution of HDAC3 regulated by actomyosin contractility. *Proceedings of the National Academy of Sciences* **110**, 11349-11354 (2013).

72. Hassinger, J.E., Oster, G., Drubin, D.G. & Rangamani, P. Design principles for robust vesiculation in clathrin-mediated endocytosis. *Proceedings of the National Academy of Sciences* **114**, E1118-E1127 (2017).

73. Sriram, K., Laughlin, J.G., Rangamani, P. & Tartakovsky, D.M. Shear-induced nitric oxide production by endothelial cells. *Biophysical Journal* **111**, 208-221 (2016).

74. Chabanon, M., Stachowiak, J.C. & Rangamani, P. Systems biology of cellular membranes: a convergence with biophysics. *Wiley Interdisciplinary Reviews: Systems Biology and Medicine* (2017).

75. Rangamani, P., Levy, M.G., Khan, S. & Oster, G. Paradoxical signaling regulates structural plasticity in dendritic spines. *Proceedings of the National Academy of Sciences* **113**, E5298-E5307 (2016).

76. Qin, D., Xia, Y. & Whitesides, G.M. Soft lithography for micro-and nanoscale patterning. *Nature protocols* **5**, 491-502 (2010).

77. Calizo, R.C. & Scarlata, S. A role for G-proteins in directing G-protein-coupled receptor–caveolae localization. *Biochemistry* **51**, 9513-9523 (2012).

78. Hanson, H.H., Reilly, J.E., Lee, R., Janssen, W.G. & Phillips, G.R. Streamlined embedding of cell monolayers on gridded glass-bottom imaging dishes for correlative light and electron microscopy. *Microscopy and Microanalysis* **16**, 747-754 (2010).